



# High oxygen reduction activity of few-walled carbon nanotubes with low nitrogen content



Maryam Borghei<sup>a,\*</sup>, Petri Kanninen<sup>b</sup>, Meri Lundahl<sup>b</sup>, Toma Susi<sup>c</sup>, Jani Sainio<sup>a</sup>, Ilya Anoshkin<sup>a</sup>, Albert Nasibulin<sup>a</sup>, Tanja Kallio<sup>b</sup>, Kaido Tammeveski<sup>d</sup>, Esko Kauppinen<sup>a</sup>, Virginia Ruiz<sup>e</sup>

<sup>a</sup> School of Science, Aalto University, FI-00076 Aalto, Espoo, Finland

<sup>b</sup> School of Chemical Technology, Aalto University, FI-00076 Aalto, Espoo, Finland

<sup>c</sup> Universität Wien, Fakultät Physik, Strudhofgasse 4, A-1090 Wien, Austria

<sup>d</sup> Institute of Chemistry, University of Tartu, 50411 Tartu, Estonia

<sup>e</sup> IK4-CIDETEC, E-20009 Donostia-San Sebastián, Spain

## ARTICLE INFO

### Article history:

Received 20 January 2014

Received in revised form 7 April 2014

Accepted 15 April 2014

Available online 24 April 2014

### Keywords:

Nitrogen-doped

Few-walled carbon nanotubes

Oxygen reduction reaction

Alkaline fuel cell

## ABSTRACT

Nitrogen-containing few-walled carbon nanotubes (N-FWCNTs) with very low nitrogen content (0.56 at.%) were obtained by a process involving the coating of acid functionalized FWCNTs with polyaniline (PANI) followed by pyrolysis at high temperatures. The resulting N-FWCNTs exhibited a remarkable electrocatalytic activity for the oxygen reduction reaction (ORR), despite significantly lower nitrogen content than previously reported in literature. The N-FWCNTs performed on par or better than Pt-C in the cathode of an alkaline direct methanol fuel cell, corroborating the ORR activity observed in the electrochemical cell and exhibiting a higher methanol tolerance. Interestingly, N-FWCNTs showed a high activity for the hydrogen evolution reaction and for the hydrogen peroxide decomposition, suggesting that the active sites involved in ORR can simultaneously catalyze other reactions. This unprecedentedly high activity for such a low N-content can be explained by the exceptional accessibility for the catalytic sites located in open and porous N-doped layer surrounding the FWCNT core, along with the minimization of inactive inner volume and mass compared to larger nitrogen doped multiwalled tubes.

© 2014 Elsevier B.V. All rights reserved.

## 1. Introduction

Improving catalyst materials for the oxygen reduction reaction (ORR) is one of the main issues in the development of low temperature fuel cells. Worldwide commercialization of fuel cells still remains a challenge due to the limited resources and high cost of platinum (Pt) as well as durability issues and CO poisoning of the Pt catalysts [1,2]. Recent advances in anion exchange membrane fuel cells (AEMFCs) have attracted considerable attention due to the potential use of less-expensive non-noble metal catalysts, which exhibit facile reaction kinetics in alkaline media [3,4]. Research on metal-free catalysts for ORR has thus become

a very active topic in catalysis, especially with the emergence of nitrogen-doped carbon nanomaterials as one of the promising electrocatalysts. Recent research has investigated nitrogen doping of different carbon nanomaterials (CNM) such as carbon nanotubes (CNTs) [5–14], carbon nanofibers (CNFs) [15,16], graphene [17,18], mesoporous carbon [19], carbon nanocages [20], and hollow carbon nanoparticles [21]. The studies are particularly numerous for nitrogen-doped CNTs (N-CNTs) among these materials. N-CNTs can also effectively catalyze other reactions, such as decomposition of H<sub>2</sub>S to solid sulfur, and the oxidative dehydrogenation of aromatic and alkanes [22,23]. Introducing nitrogen atoms into the CNT structure effectively modulates their chemical reactivity, electron-donor ability and electrochemical properties [24]. Nitrogen dopants can shift the Fermi level to the conduction band, causing the semi-conducting CNTs to exhibit metallic properties [25]. Moreover, the addition of nitrogen to the CNT wall changes the charge distribution of the nanotube so that C atoms adjacent to N become more

\* Corresponding author. Tel.: +358 503608519; fax: +358 947023517.

E-mail addresses: [maryam.borghei@aalto.fi](mailto:maryam.borghei@aalto.fi), [maryam.borghei@gmail.com](mailto:maryam.borghei@gmail.com) (M. Borghei).

positively charged, resulting in an enhanced interaction with the adsorbed molecules and lower activation barrier for their decomposition [26].

N-CNTs can be obtained by either in situ doping during the CNT synthesis, or by post-treatment of as-synthesized CNTs with nitrogen-containing precursors. During in situ doping, nitrogen atoms derived from different precursors such as transition metal macrocycles [5], ammonia [6], acetonitrile [7,11], pyridine [8,9], melamine [10] and polymers [27,28] are incorporated into the carbon network simultaneously as CNTs grows. It has been reported that the presence of metals originating from a typically metal-catalyzed synthesis process can contribute to ORR catalysis [29]. To avoid misidentifying the origin of ORR activity catalyst metal residues should be removed before electrochemical measurements. However, any acid leaching to remove metals may damage nitrogen functionalities. Post-treatment methods typically avoid this difficulty by treating already purified CNTs with nitrogen precursors; such as ammonia [11], urea [14], dicyandiamide [30], or polymers including polyaniline (PANI) [13] and polypyrrole [16].

PANI offers several advantages among nitrogen-containing polymers; it is an outstanding conductive polymer with low price, good processability, controllable and stable conductivity over a wide potential range [31–33]. Moreover, PANI conjugated groups can interact strongly with the CNT walls to provide core–shell composite structures (CNT–PANI) with enhanced synergic properties [34]. The core–shell structure of CNT–PANI is expected to be formed via the strong  $\pi$ – $\pi$  conjugation of the quinoid rings of PANI and the benzenoid rings of CNTs. On the other hand, the CNT core structure has a significant influence on the properties of the final composite such as charge-transfer, catalytic activity, and bulk conductivity. Few-walled CNTs (FWCNTs) have been recently proposed as an intermediate between single-walled CNTs (SWCNTs) and multi-walled CNTs (MWCNTs), displaying the appropriate combination of structural perfection and remarkable electronic properties [35]. Most importantly in this context, only layers accessible to the electrolyte will contribute to the electrochemical activity. While the conductivity of N-SWCNTs is dramatically lowered by doping due to the perturbation of the quasi-1D channel of the tubes by the charged dopants [6,36], using FWCNTs minimizes the volume and mass of the inactive inner layers but still retains the required good conductivity.

In this work, high quality FWCNTs of 2–5 walls were synthesized by chemical vapor deposition (CVD), carefully purified, functionalized and subsequently coated with PANI and carbonized at high temperatures. The obtained nitrogen-containing FWCNTs (N-FWCNTs) with only about 0.5 at.% nitrogen showed a remarkable high electrocatalytic activity toward ORR. Its high electrocatalytic activity examined both in an electrochemical cell and an alkaline methanol fuel cell. To the best of our knowledge, such a high electrocatalytic activity of N-CNT catalyst with this low nitrogen content has not been previously observed. The results of this work imply that other parameters than only the nitrogen content should be also considered for a good ORR electrocatalytic activity of N-CNTs, as discussed in Section 4.

## 2. Experimental

### 2.1. Catalyst preparation

FWCNTs were synthesized by catalytic pyrolysis of methane ( $\text{CH}_4$ ) diluted with hydrogen ( $\text{H}_2$ ) at 950 °C on cobalt–molybdenum (CoMo) oxides (5 at.%) supported on magnesium oxide (MgO) [37]. After synthesis, residual metal catalysts were removed by hydrochloric acid (HCl), rinsed properly with deionized water and dried in vacuum. In order to investigate the effect of pre-treatment

on the final doping level, a part of FWCNTs were subject to oxidative functionalization in 2 M  $\text{HNO}_3$ /1 M  $\text{H}_2\text{SO}_4$  (1:1) solution under reflux conditions at 120 °C for 4 h. PANI was deposited both on the functionalized and the merely purified FWCNTs by the chemical oxidative polymerization of aniline monomers [38]. FWCNTs (0.5 g) were suspended in 1 M HCl (100 ml) and sonicated for a good dispersion. The aniline monomer (0.15 g) in 1 M HCl was added dropwise into the suspension and stirred for 1 h. The oxidizing agent ammonium persulfate ( $(\text{NH}_4)_2\text{S}_2\text{O}_8$ , APS) was dissolved in 1 M HCl and added dropwise (1:1 mass ratio of APS to aniline) under constant vigorous stirring in an ice bath (at 0 °C). The mixture was stirred for 6 h to achieve a good degree of polymerization. Finally, the reaction was terminated by the addition of acetone. The resulting products were filtered, washed with deionized water, and dried in vacuum. Then PANI-FWCNTs composites were pyrolyzed for 1 h at 600 °C and 900 °C in an argon flow to obtain N-FWCNTs. The samples are coded as follows: FW-Pr for the merely purified FWCNTs, FW-F for the functionalized FWCNTs, NFW-Pr-900 for the N-FWCNTs pyrolyzed at 900 °C using purified FWCNTs, and NFW-F-600 and NFW-F-900 for the N-FWCNTs pyrolyzed at 600 and 900 °C, respectively using the functionalized FWCNTs.

### 2.2. Physical characterizations

Scanning electron microscopy (SEM) was carried out with a JEOL field emission microscope JSM-7500FA equipped with an energy dispersive X-rays spectrometer (EDXS). High resolution transmission electron microscopy (HR-TEM) was conducted with a JEOL double Cs-corrected TEM (JEM-2200FS) operated at an acceleration voltage of 200 kV. Raman analysis was performed using a Horiba LabRAM HR spectrometer equipped with a CCD camera and a 633 nm excitation laser. X-ray photoelectron spectroscopy (XPS) was carried out with a Surface Science Instruments SSX-100 ESCA spectrometer using monochromatic  $\text{AlK}_{\alpha}$  X-rays and an electrostatic hemispherical analyzer. The spectra were recorded with pass energy of 100 eV and an X-ray spot size of 600  $\mu\text{m}$ .

### 2.3. Electrochemical characterizations

Glassy carbon electrodes (GCE, 0.196  $\text{cm}^2$ ) were polished and dried. The working electrode was prepared as follows: 5 mg of the catalyst powder, 476  $\mu\text{l}$  of ethanol, and 24  $\mu\text{l}$  of FAA3 anion exchange ionomer (solution of 12 wt.% FAA3 in N-methyl-2-pyrrolidone (NMP), supplied by Fuma-Tech) were mixed for 2 h and sonicated to form a uniform catalyst ink. Then a 7  $\mu\text{l}$  drop of ink was carefully deposited on the GCE. The electrochemical characterization was performed in a conventional three-electrode cell comprising the modified GCE as working electrode, Pt wire as counter electrode, and Ag/AgCl/3 M KCl as the reference electrode (RE) using an Autolab PGSTAT12 potentiostat controlled by the GPES software. All potentials reported in this study were referenced to that of the Ag/AgCl electrode. The ORR measurements were carried out in an  $\text{O}_2$  saturated 0.1 M KOH solution at room temperature. Cyclic voltammetry (CV) experiments were carried out in a potential range from 0.2 to  $-1.2$  V at  $10 \text{ mV s}^{-1}$  scan rate. In order to evaluate the reproducibility of the electrochemical measurements three electrodes were prepared with each catalyst sample and the relative standard deviation (R.S.D.) of the peak current density was around 5%. The batch-to-batch repeatability was slightly lower, with a R.S.D. of 8–10%. Rotating disk electrode (RDE) measurements were performed at  $5 \text{ mV s}^{-1}$  scan rate and different rotation speeds ( $\omega$ ) from 100 to 3600 rpm. Rotating-ring disk electrode (RRDE) experiments were performed using the RRDE setup from Pine Research Instrumentation. The disk potential was scanned at  $5 \text{ mV s}^{-1}$  while the Pt ring electrode potential was fixed at 0.5 V. The

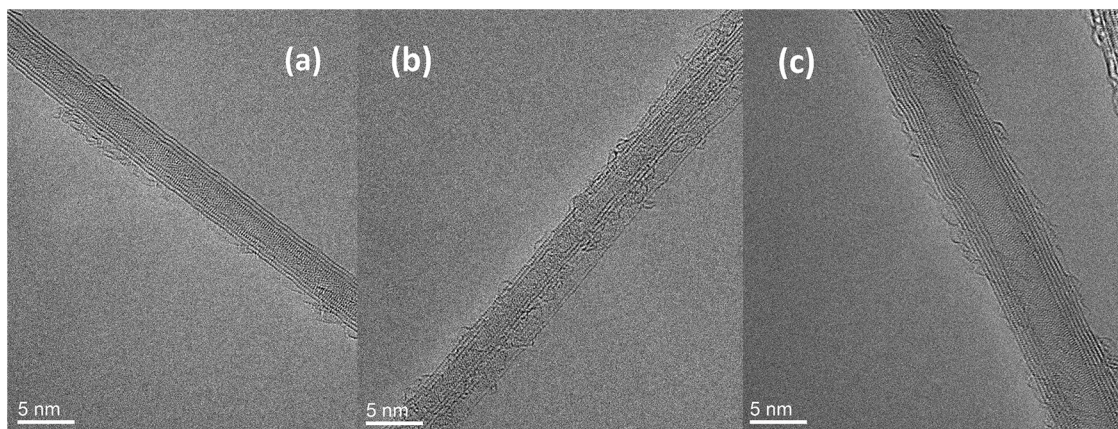


**Fig. 1.** HR-TEM images of FWCNTs, PANI-FWCNTs and N-FWCNTs.

ORR activity of a commercial Pt-C catalyst (E-TEK, 20 wt.% Pt supported on Vulcan XC-72) was also evaluated for comparison with N-FWCNTs. The electrocatalytic activity of N-FWCNTs toward the decomposition of  $\text{H}_2\text{O}_2$  was measured to evaluate kinetic parameters from the Tafel plots. The electrolyte was first saturated with  $\text{N}_2$  and then  $10\ \mu\text{l}$  of 1 M  $\text{H}_2\text{O}_2$  was injected with a microsyringe into the cell while electrode was rotating at 1500 rpm. After 1 min, a linear sweep from the open circuit voltage (OCV) to  $-0.4\text{ V}$  at a  $0.17\text{ mV s}^{-1}$  scan rate was made. After the reduction sweep, the electrolyte was replaced and the procedure was repeated for the oxidation sweep from OCV to  $+0.4\text{ V}$ .

#### 2.4. Alkaline fuel cell measurements

Direct methanol alkaline fuel cell tests were conducted using a homemade fuel cell stack ( $5.29\text{ cm}^2$  active area). Membrane-electrode assemblies (MEA) were fabricated using FAA3 membrane (Fuma-Tech) and diffusion layers containing microporous layer (FuelCellEtc GDL-CT). FAA3 membrane was pretreated in 0.5 M NaOH to exchange  $\text{Br}^-$  ions with  $\text{OH}^-$ . The catalyst inks were prepared by mixing isopropanol and FAA3 ionomer solution, then sprayed on the diffusion layers by air brush and dried in vacuum. N-FWCNT catalyst loading at the cathode was  $2.2\text{ mg cm}^{-2}$ . A reference MEA was also prepared for the cathode using commercial Pt supported on a high surface area carbon (Alfa Aesar, 60 wt.% Pt) and Pt loading was  $0.5\text{ mg cm}^{-2}$ . At the anode, PtRu supported on high surface area carbon (Alfa Aesar, 40 wt.% Pt and 20 wt.% Ru) was used with higher PtRu loading  $3.0\text{ mg cm}^{-2}$  to ensure that catalytic activity of the fuel cell is not limited by the anode. Our results [39] have shown that with such MEA composition, the DMFC performance is under cathode control. Prior to the fuel cell measurements, the assembly was stabilized overnight. Polarization curves were recorded at  $50^\circ\text{C}$  by passing a methanol flow ( $2.0\text{ ml min}^{-1}$ ) at the anode and an oxygen flow ( $200\text{ ml min}^{-1}$ ) at the cathode while sweeping the potential from the open circuit voltage (OCV) to  $0.05\text{ V}$  at a  $2\text{ mV s}^{-1}$  scan rate.

### 3. Results

#### 3.1. Physical characterizations of catalysts

Surface morphologies of pristine FWCNTs, the PANI-FWCNTs composite, and the final pyrolyzed N-FWCNTs are shown in HR-TEM micrographs in Fig. 1. FWCNTs (Fig. 1a) consist of 2–5 walls with a highly crystalline structure and about  $1\ \mu\text{m}$  in length. Fig. 1b shows clearly an additional polymer layer, resembling a narrow strip wrapping around the nanotube. Oxidation of aniline

is a typical redox reaction, in which electrons from aniline are withdrawn by an oxidant. FWCNTs work as electron transfer mediator between the reductant (aniline) and the oxidant (APS). The aniline monomer/oligomers are first adsorbed on the surface of FWCNTs, and then polymer starts to grow as the reaction proceeds [34]. After carbonization at a high temperature, a very thin layer of N-doped graphitized carbon is formed on the nanotube walls (Fig. 1c). The images reveal that the surface modification was accomplished without introducing major defects in the FWCNT structure. This is crucial for maintaining the desired intrinsic properties of the nanotubes.

Raman spectra of the samples are shown in Fig. 2 and the corresponding data presented in Table 1. The D-band around  $1350\text{ cm}^{-1}$  is the characteristic mode for defective structures, and the G-band around  $1580\text{ cm}^{-1}$  corresponds to graphitic layers [40]. The low intensity ratio of the D to G band ( $I_D/I_G$ ) for the pristine FWCNTs (0.31) indicates a highly ordered structure of the nanotubes. The slightly higher  $I_D/I_G$  for the functionalized FWCNTs (0.37) can be ascribed to defects resulting from the acid treatment, corroborated by higher oxygen content (from XPS data, Table 1). A relatively small decrease and shift of the second-order D'-band is also observed for the functionalized (Fig. 2), and the polymer-coated FWCNTs (Fig. S1).

Raman spectra are very sensitive to the interaction between the FWCNTs and PANI, as shown in Fig. S1. PANI oxidation state

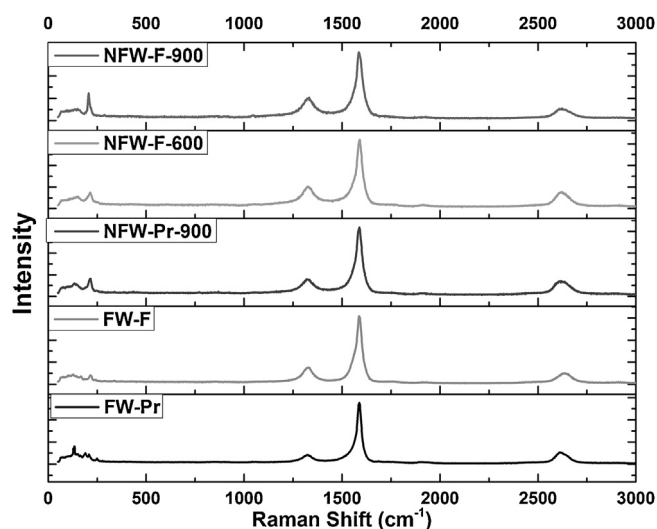


**Fig. 2.** Raman spectra of the FW-Pr, FW-F, NFW-900, NFW-F-600 and NFW-F-900 samples.



**Table 1**  
Raman spectroscopy and XPS data analysis.

	FW-Pr	FW-F	NFW-F-600	NFW-F-900	NFW-Pr-900
$I_D/I_G$	0.31	0.37	0.48	0.22	0.24
O (at.%)	1.2	3.7	0.8	0.87	0.36
N (at.%)	–	–	0.72	0.56	0.27
Pyridinic-N (%)	–	–	28	35	31
Pyrrolic-N (%)	–	–	44	8	8
Graphitic-N (%)	–	–	20	44	46
Pyridine-N-oxide (%)	–	–	8	13	15

can be identified to be conducting *emeraldine* form due to the appearance of bands in the region between  $1000$  and  $1700\text{ cm}^{-1}$ . The presence of various torsion angles and twisting of the aniline rings in the polymer layer are also suggested by Raman bands located between  $300$  and  $1000\text{ cm}^{-1}$ . After the composite pyrolysis at  $900^\circ\text{C}$ ,  $I_D/I_G$  ratio is significantly reduced ( $0.23 \pm 0.01$ ), suggesting a higher degree of graphitization. However, a less ordered structure ( $I_D/I_G = 0.48$ ) was obtained for the sample pyrolyzed at  $600^\circ\text{C}$ .

XPS measurements were carried out in order to analyze the elemental composition of the samples and to investigate the binding configurations of nitrogen atoms in N-FWCNTs. The XPS survey spectrum (Fig. S2) of the NFW-F-900 sample shows a dominant narrow graphitic C 1s peak at  $284.4\text{ eV}$ , and some oxygen. The nitrogen content is too low, to be visible in low resolution spectra. The nitrogen atomic concentrations derived from high resolution spectra and the N 1s peak are  $0.72\text{ at.}\%$  for NFW-F-600,  $0.56\text{ at.}\%$  for NFW-F-900 and only  $0.27\text{ at.}\%$  for NFW-Pr-900 sample. Both oxygen and nitrogen contents are slightly increased in the sample produced from the functionalized FWCNTs (NFW-F-900) compared to the untreated one (NFW-Pr-900) (Table 1). The higher nitrogen concentration is likely due to a stronger interaction of PANI with the functionalized FWCNTs. Nitrogen content is slightly decreased with increasing pyrolysis temperature from  $600^\circ\text{C}$  to  $900^\circ\text{C}$ , possibly due to the loss of nitrogen-containing gases.

The XPS high resolution N 1s spectra of N-FWCNTs with the curve deconvolution are shown in Fig. 3. The deconvolution was done by assuming a commonly used scheme with four peaks corresponding to pyridinic-N (at ca.  $398.3\text{ eV}$ ), pyrrolic-N (at ca.  $400.1\text{ eV}$ ), graphitic-N (or quaternary-N) (at ca.  $400.9\text{ eV}$ ) and pyridinic N-oxide (at ca.  $403.5\text{ eV}$ ) bonding configurations [11,20]. For the three N-FWCNTs samples, pyridinic-N content is rather similar ( $32 \pm 3\%$ ). However, pyrrolic-N content is the highest in NFW-F-600 ( $43.7\%$ ), in contrast to samples carbonized at  $900^\circ\text{C}$  (NFW-F-900 and NW-Pr-900) with predominantly graphitic-N

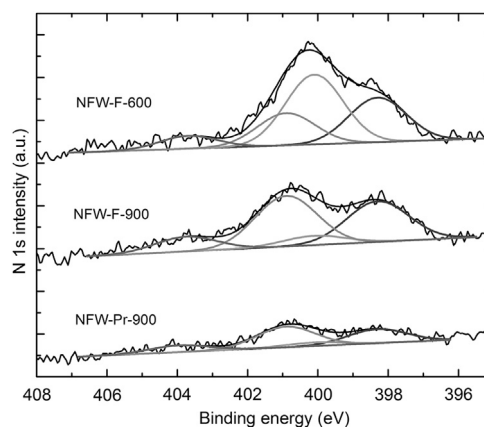


**Fig. 3.** Deconvolution of N 1s XPS spectra of the NFW-F-600, NFW-F-900, and NFW-Pr-900 samples. The peaks are color-coded as pyridinic-N (blue), pyrrolic-N (magenta), graphitic-N (red), pyridinic N-oxide (green). (For interpretation of the references to color in this figure legend, the reader is referred to the web version of this article.)

content ( $\sim 45\%$ ). It has been reported that pyrrolic-N groups transform to pyridinic-N with increasing temperature via a dynamic surface rearrangement; and by further temperature increase, the most stable graphitic-N structures are formed through ring condensation [41–43].

### 3.2. Electrochemical characterization of catalysts

The electrocatalytic activity of N-FWCNTs for ORR was investigated using GC-coated electrodes in an  $\text{O}_2$ -saturated  $0.1\text{ M KOH}$  solution. The ORR activity of a catalyst can be qualitatively inferred from the cyclic voltammograms (CVs). Fig. 4 shows CV curves of FW-Pr and NFW-F-900 samples. The featureless CV in the de-aerated ( $\text{N}_2$ -saturated) electrolyte implies that FWCNTs are well purified so that no metal catalyst residues contribute to the

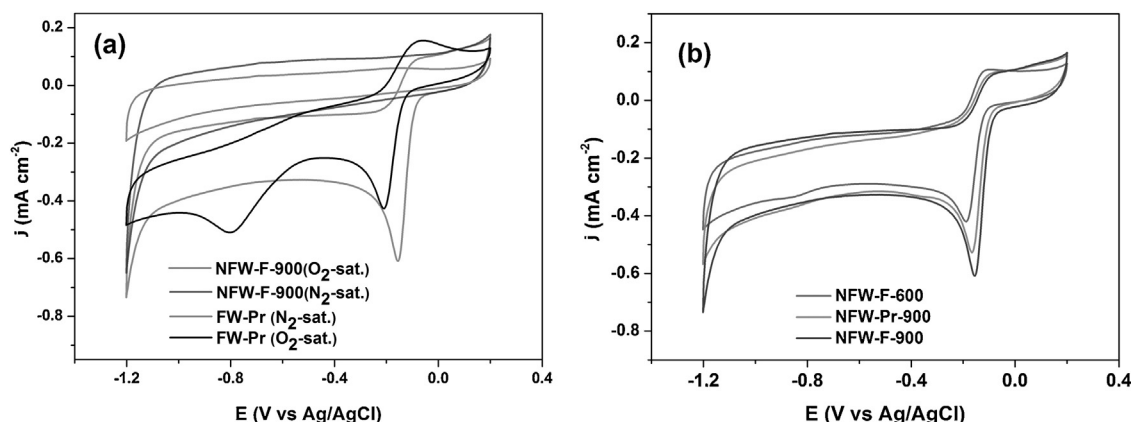


**Fig. 4.** (a) CVs of FW-Pr and NFW-F-900 in  $\text{N}_2/\text{O}_2$ -saturated  $0.1\text{ M KOH}$ , (b) CVs of N-FWCNTs in  $\text{O}_2$ -saturated  $0.1\text{ M KOH}$ ; at a  $10\text{ mV s}^{-1}$  scan rate.

**Table 2**

The onset and peak potentials for ORR obtained from CV and RDE measurements and kinetic parameters calculated from Tafel plots (Fig. 8).

	Purified	NFW-F-600	NFW-F-900	NFW-Pr-900	Pt-C
Onset potential (V) <sup>a</sup>	−0.07	−0.06	−0.03	−0.04	0.05
Peak potential (V) <sup>b</sup>	−0.2	−0.18	−0.15	−0.16	−0.15
$k$ ( $10^{-3} \text{ cm s}^{-1}$ )	–	0.4	2.8	1.6	3.1
$j_d$ ( $\mu\text{A}$ )	–	3.1	21.2	11.9	23.3
$\alpha$	–	0.2	0.42	0.36	0.49

<sup>a</sup> Onset potentials derived from LSV curves.<sup>b</sup> Peak potentials derived from CVs.

electrochemical reaction. It can be seen that ORR on FW-Pr occurs via a  $2e^-$  pathway, presenting two reduction peaks at  $-0.2$  and  $-0.8$  V. The ORR activity is greatly improved on NFW-F-900, proceeding via a  $4e^-$  pathway with only one ORR peak at  $-0.15$  V. Fig. 4b compares the CVs of the three N-FWCNTs samples (Treatment at  $600^\circ\text{C}$  improved the electrocatalytic activity compared to FW-Pr, with the peak potential shifting to more positive potentials (from  $-0.2$  to  $-0.18$  V)). Pyrolysis at  $900^\circ\text{C}$  (NFW-F-900) resulted an enhanced ORR activity, as revealed by the higher peak potential ( $-0.15$  V) and the current density. However, NFW-Pr-900 produced from un-treated FWCNTs showed an intermediate peak current density and peak potential ( $-0.16$  V). For comparison, CVs of the commercial Pt-C in de-aerated and  $\text{O}_2$ -saturated electrolyte are presented in Fig. S3, and the peak potentials are compared with those of N-FWCNTs in Table 2.

The long tail in the CV of NFW-F-900 at around  $-1.2$  V corresponds to high activity for the hydrogen evolution reaction (HER). A photograph (Fig. S4) taken during the measurements demonstrates the formation of hydrogen bubbles at the GC-modified electrode in the electrolyte. It can be seen (Fig. 4b) that the catalysts with higher ORR activity show longer tails in their CV, suggesting that the active sites involved in the ORR can simultaneously catalyze the HER at more negative potentials. Further research on N-FWCNTs for catalyzing hydrogen evolution is currently underway.

RDE experiments were carried out to evaluate ORR electrocatalytic activity and the kinetic parameters over rotation rates from 100 to 3600 rpm. Fig. 5a shows the linear sweep voltammograms (LSV) recorded for the FW-Pr and NFW-F-900 samples. It can be seen that the onset potential for ORR is significantly improved after N-doping treatment. The higher onset potential of the samples carbonized at  $900^\circ\text{C}$  compared to  $600^\circ\text{C}$  (Fig. 5b, Table 2) could be due to a higher graphitization degree of the N-doped carbon layer (in agreement with  $I_D/I_G$  values), promoting enhanced electron transfer from the catalytic sites to the electrode. In addition, the onset

potential of NFW-F-900 is further improved compared to NFW-Pr-900.

At potentials above  $-0.4$  V, ORR is in the kinetics-controlled regime, where the catalytic activity of a material is typically benchmarked. At potentials lower than  $-0.4$  V, the ORR is in the diffusion-controlled regime, where mass transfer of  $\text{O}_2$  to the electrode determines the ultimate current density. The overall current density ( $j$ ) in RDE measurements can be evaluated from the Koutecky–Levich (K–L) equation

$$\frac{1}{j} = \frac{1}{j_k} + \frac{1}{j_d} = \frac{1}{j_k} + \frac{1}{0.62nFD_{\text{O}_2}^{2/3}\nu^{-1/6}C_{\text{O}_2}^b\omega^{1/2}} \quad (1)$$

where  $j_k$  is the kinetic current density,  $j_d$  is the diffusion-limited current density,  $F$  is the Faraday constant ( $96486.4 \text{ C mol}^{-1}$ ),  $D$  is the diffusion coefficient of oxygen in water ( $1.9 \times 10^{-5} \text{ cm}^2 \text{ s}^{-1}$ ),  $C$  is the concentration of  $\text{O}_2$  ( $1.2 \times 10^{-6} \text{ mol cm}^{-3}$ ),  $\nu$  is the kinematic viscosity of water ( $0.01 \text{ cm}^2 \text{ s}^{-1}$ ), and  $\omega$  is the electrode rotation rate ( $\text{rad s}^{-1}$ ). The number of transferred electrons ( $n$ ) can be obtained using K–L plots ( $j^{-1}$  vs  $\omega^{-1/2}$ ) and the slope of extrapolated lines at different potentials.

The corresponding K–L plots for FW-Pr and NFW-F-900 at various potentials are shown in Fig. 6. They exhibit good linearity for the samples, indicating first-order reaction kinetics for ORR [44]. The inset in Fig. 5b shows the electron transfer number calculated from the slope of K–L plots at different potentials. The average  $n$  value obtained in the potential range from  $-0.3$  to  $-0.5$  V is 2.1 for FW-Pr and 3.1 for NFW-F-600, whereas NFW-F-900 is significantly enhanced to 4.0, and NFW-Pr-900 to an intermediate value  $n = 3.5$ .

We further investigated ORR electrocatalytic activity by measuring the disk and the Pt-ring currents in RRDE for the best performing N-FWCNTs (NFW-F-900) and compared their activity with FW-Pr and commercial 20 wt.% Pt-C. As presented in Fig. 7a and Table 2, although the on-set potential at NFW-F-900 is lower than that of

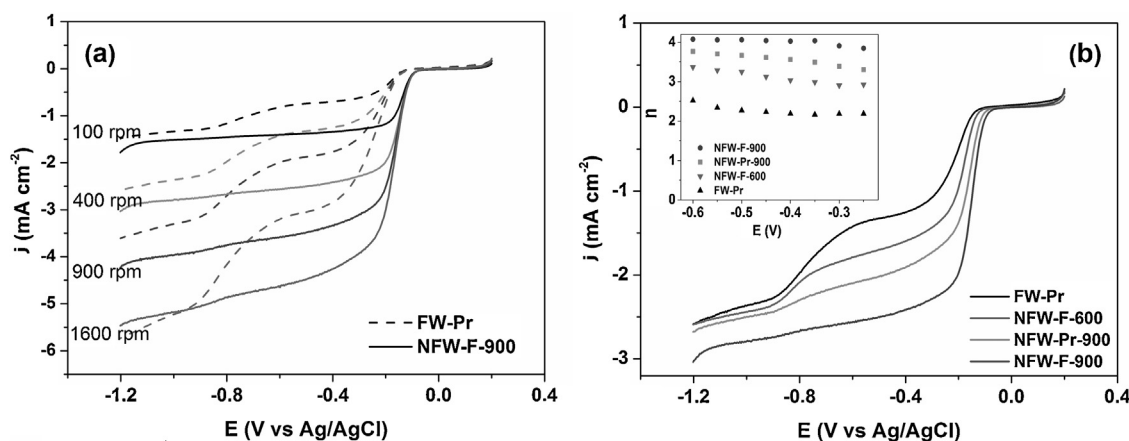


**Fig. 5.** (a) LSV of FW-Pr and NFW-F-900 at rotation rates from 100 to 1600 rpm, (b) LSV of N-FWCNTs at 400 rpm (in  $\text{O}_2$ -saturated 0.1 M KOH at  $5 \text{ mV s}^{-1}$  scan rate), inset: electron transfer number at different potential derived from K–L plots.

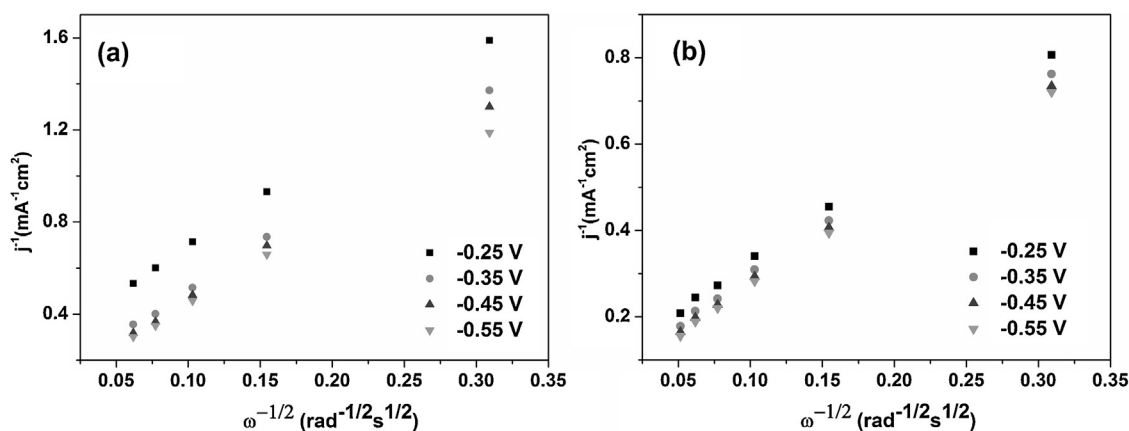


Fig. 6. Koutecky–Levich plots for oxygen reduction on (a) FW-Pr and (b) NFW-F-900 in 0.1 M KOH. Data derived from Fig. 5a.

Pt-C electrode, it was significantly higher than that of FW-Pr despite their low nitrogen content.

Here,  $n$  and  $\text{H}_2\text{O}_2\%$  were calculated from the following equations:

$$n = \frac{4I_d}{I_d + \frac{I_r}{N}} \quad (2)$$

$$\text{H}_2\text{O}_2\% = \frac{4 - n}{2} \times 100 \quad (3)$$

where  $N$  is the collection efficiency (0.24),  $I_d$  and  $I_r$  are the currents at the GC-disk and the Pt-ring, respectively. The corresponding transferred electron number and  $\text{H}_2\text{O}_2$  production in the whole potential range are illustrated in Fig. 7b. The results show that the ORR activity of the NFW-F-900 is greatly improved to 3.72 electrons transferred at  $-0.4$  V and 87% conversion of oxygen molecules to  $\text{OH}^-$ , indicating that an efficient  $4e^-$  pathway is the dominant reaction mechanism. The performance of NFW-F-900 with such low nitrogen doping becomes very close to that of Pt-C, with 3.9 transferred electrons at  $-0.4$  V and 98% selectivity for  $\text{OH}^-$  formation.

The electrocatalytic activity of the modified-GC electrodes was further characterized to investigate kinetic parameters of the decomposition of  $\text{H}_2\text{O}_2$ . Fig. 8 shows the Tafel plots obtained after the injection of hydrogen peroxide and scanning in the  $\text{OCV} \pm 0.4$  V potential ranges. In a Tafel plot, there is an anodic branch with slope of  $(1 - \alpha)F/2.3RT$  and a cathodic branch with slope of  $-\alpha F/2.3RT$ . Then the transfer coefficient,  $\alpha$  (a measure of the symmetry of the energy barrier), can be calculated using the slopes [45]. The

oxidation reaction is a slow process when  $\alpha$  values are higher than 0.5, while  $\alpha$  values lower than 0.5 indicate a slow reduction reaction. The heterogeneous reaction rate can be calculated from the equation:

$$-\left. \frac{d[\text{H}_2\text{O}_2]}{dt} \right|_{\text{surface}} = \frac{|j_d|}{nF} = k[\text{H}_2\text{O}_2] \quad (4)$$

where  $j_d$  is the exchange current density of the redox reaction obtained from the y-intercept between the oxidation and reduction slopes of the Tafel plots (presented in Table 2),  $[\text{H}_2\text{O}_2]$  is the initial concentration of hydrogen peroxide (0.4 mM). Taking  $n=2$  for FWCNTs, and  $n=1$  for the N-FWCNTs and Pt-C; as previously reported by Wiggins-Camacho and Stevenson [29]  $k$  can be calculated. The kinetic rate constants obtained for heterogeneous  $\text{H}_2\text{O}_2$  decomposition on the samples follow the same trend as ORR activity: Pt-C > NFW-F-900 > NFW-P-900 > NFW-F-600 (Table 2). Specifically, NFW-F-900 with  $k=2.8 \times 10^{-3} \text{ cm s}^{-1}$  performed very similarly to that of Pt-C electrode ( $3.1 \times 10^{-3} \text{ cm s}^{-1}$ ), supporting the RRDE measurements. The same trend can also be observed with  $\alpha$  values obtained for the above samples. As can be seen, more symmetrical Tafel plots are obtained for both Pt-C and NFW-F-900 as  $\alpha$  values approach to 0.5 (Table 2). Likewise, a correlation between the ORR electrocatalytic activity and the activity of  $\text{H}_2\text{O}_2$  disproportionation was previously observed on non-noble metal catalysts (NMC) such as Fe/N/C [29,46]. Our rate constant values are in agreement with those of Dodelet et al., who predicted a rate constant in the order of  $10^{-3} \text{ cm s}^{-1}$  at 1500 rpm, both experimentally and theoretically [46]. The high electrocatalytic activity of N-FWCNTs

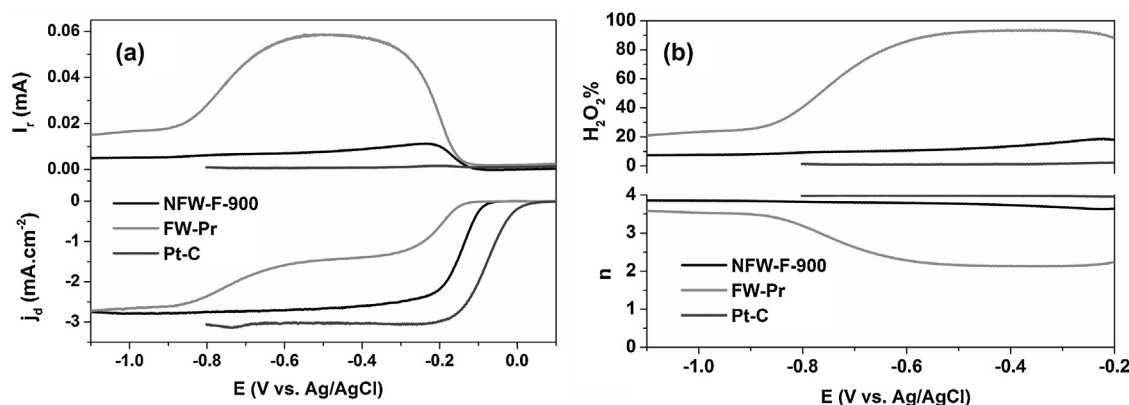
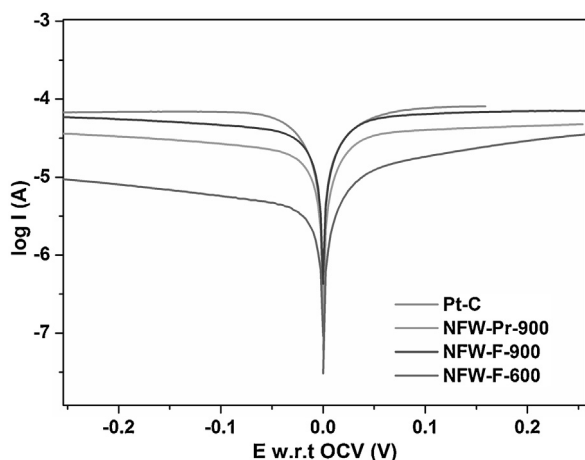


Fig. 7. (a) Disk and Pt-ring current density, (b)  $\text{H}_2\text{O}_2\%$  and number of transferred electrons, for FW-Pr, NFW-F-900 and Pt-C;  $5 \text{ mV s}^{-1}$  scan rate and 400 rpm in  $\text{O}_2$ -saturated 0.1 M KOH.



**Fig. 8.** Tafel plots derived from the polarization curves of Pt-C, NFW-Pr-900, NFW-F-900 and NFW-F-600 at a scan rate of  $0.17 \text{ mV s}^{-1}$  and a rotation rate of 1500 rpm in  $\text{N}_2$ -saturated  $0.1 \text{ M KOH}$  containing  $0.4 \text{ mM H}_2\text{O}_2$ .

toward the reduction of hydrogen peroxide makes this material useful for biosensing applications where  $\text{H}_2\text{O}_2$  needs to be detected as by-product of biomolecule reactions [47].

### 3.3. Fuel cell measurements

Finally, performance of the NFW-F-900 sample was evaluated in an alkaline direct methanol fuel cell (DMFC) to compare its electrocatalytic activity with that of a commercial Pt-C cathode. The polarization curves and power density of the NFW-F-900 and Pt-C catalysts are shown in Fig. 9. Surprisingly, NFW-F-900 outperforms the Pt-C catalyst at low and medium current densities, and then gradually reaches almost identical performance in the high current density region. The OCV obtained with NFW-F-900 is significantly higher ( $0.50 \text{ V}$ ) than that of Pt-C ( $0.44 \text{ V}$ ). The lower OCV for the Pt-C catalyst can be due to methanol cross over, causing a mixed potential at the cathode. The higher tolerance of N-FWCNTs to methanol cross-over was verified by the electrooxidation of methanol ( $3 \text{ M}$ ) in an electrochemical cell containing  $\text{O}_2$ -saturated  $0.1 \text{ M KOH}$  electrolyte (Fig. S5). The maximum power density of  $0.75 \text{ mW cm}^{-2}$  obtained by NFW-F-900 is slightly higher than that of Pt-C ( $0.70 \text{ mW cm}^{-2}$ ). Although the overall cell performance is rather low due to the type of membrane (FAA3) and the fuel cell configuration, N-FWCNTs demonstrate comparable activity with the Pt-C. On the other hand, the results of this work represent a 2.5-fold increase in power density compared to our previous study using a FAA2 (Fuma-Tech) membrane at  $30^\circ\text{C}$  [48]. It is worth pointing out that anion exchange membrane technology is still at its infancy and further developments are required for them to compete with the more mature proton exchange membrane technology.

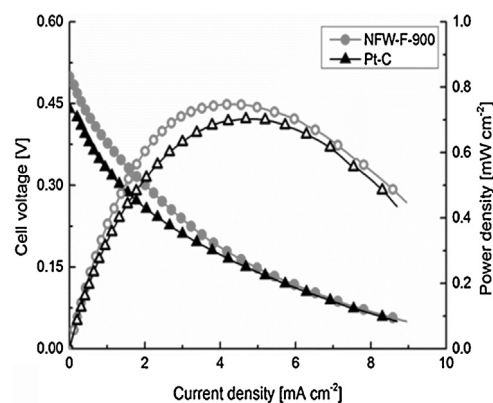


**Fig. 9.** Polarization curves and power densities of the NFW-F-900 and Pt-C catalysts in a fuel cell test.

Further characterization on the influence of FAA3 ionomer content on the cathode electrode structure and overall alkaline DMFC performance is presented in another study by Kanninen et al. [39].

## 4. Discussions

To the best of our knowledge, such a remarkable high electrocatalytic activity has not been previously reported for N-CNT catalysts with such a low N content of about  $0.5\%$ . The exact role of nitrogen doping for the ORR activity of N-doped carbon nanomaterials is currently under debate. Wiggins-Camacho and Stevenson et al. [24] investigated the effect of doping on the physicochemical properties of CNTs and reported that the density of states increased gradually with N-doping level from  $4$  to  $7.4 \text{ at.}\%$ , along with the ORR activity [29]. They also reported that the density of states increased predominantly with pyridinic-N content, facilitating the formation of a localized donor state close to the Fermi level. A direct correlation between the ORR activity and the N-doping level has also been reported by other groups [49,50]. However, this subject is controversial, as others have found that there is no correlation between total nitrogen content and the ORR electrocatalytic activity [11,51]. For instance, N-CNTs synthesized via the direct decomposition of melamine, with nitrogen doping level as high as  $20 \text{ at.}\%$ , showed very low ORR activity with only  $2.6$  transferred electrons [52]. In this case, nitrogen atoms were concentrated at the curved joints of bamboo-like compartments (trapped between the graphitic walls); thus most of them were not accessible to oxygen molecules for the reaction. It is also possible that nitrogen gas is encapsulated in the bamboo-like compartments during CVD synthesis and is not active site any more [53]. Table 3 compares results found in the literature with our NFW-F-900 catalyst. It can be seen that for an acceptable ORR activity ( $n > 3.5$ ), a nitrogen content higher than  $3 \text{ at.}\%$  is

**Table 3**  
Comparison of N-CNT catalysts reported in literature with our N-FWCNTs.

Method	N-precursor	$n_e$	Onset, peak potential (V)	Total N (at.%)	Predominant N group	Diameter (nm)	Ref.
In situ synthesis	Iron(II) phthalocyanine	3.9	$0.02, -0.15$	4–6	Substitutional N with 3-SW defects	25	[5]
	Melamine	2.6	$-0.1, -0.27$	20	Pyridinic	40–60	[49]
	Pyridine	2.76–3.63	$-0.1, -$	2.51–3.28	Quaternary/pyrrolic	30–60	[46]
	Poly(2-methyl-1-vinylimidazole)	3.8	$-0.05, -$	$\sim 8$	Pyridinic	100	[27]
	Pyridine	2.7–3	$-0.1, -0.2$	3–6	Quaternary (valley)	25–50	[38]
Post-treatment	Polymers	–	–, –	4.3–10.7	Pyridinic	100	[26]
	Ammonia	–	$0.05, -$	2.9–6	Graphitic	70–200	[11]
	Polyaniline	–	–, –	7.6–3.3	Graphitic	70–200	[13]
	Urea	3–3.5	$-0.05, -0.2$	5	Pyridinic	10–15	[14]
	Polyaniline	3.74	$-0.03, -0.15$	0.56	Graphitic	1.8–7.7	This work



usually required. However in this work, a high ORR activity is obtained despite almost six-times lower nitrogen loading.

The difference may arise from the structure of the N-doped graphitic layer attached to our nanotube walls. It can be seen that the N-doped layer (Fig. 1c) forms an open porous structure with abundant edge planes and defects attached to the FWCNT core. Nitrogen sites on defects and edge locations are likely more reactive and more accessible for oxygen molecules, while the highly conductive FWCNT cores convey charge efficiently along tube axis. Oh et al. studied the influence of the carbon support structure on post-doping with nitrogen-containing precursors. They reported that unlike the basal plane, nitrogen incorporation into disorder and edge plane locations provides an appropriate geometry, facilitating the ORR by promoting more favorable active site exposure [51]. Our efforts to elucidate the location of nitrogen atoms with electron energy loss spectroscopy (EELS) could not provide solid information due to very low nitrogen signal and the interference of the noise level on the spectrum. However despite the low N-content, the limiting current density of oxygen reduction on NFW-F-900 is also remarkably close to that of Pt-C (Fig. 7a). It is established that a high current density is result of a combined high turnover frequency (the number of reactions occurring at a specific site per second), high conductivity of the catalyst support to conduct electrons to/from the catalytic sites, and the electron transfer number ( $n$ ) of the oxygen reduction pathway [54]. Previously, Dodelet and co-workers reported that for non-noble metal catalysts prepared using post-treatment of carbon black via pyrolysis of  $\text{NH}_3$ , the micropore surface area of the resulting catalyst governed the catalytic activity, rather than nitrogen content [55,56]. Therefore, in addition to the total N-content, other parameters should be simultaneously considered to explain the ORR activity of an N-doped carbon material. Among them, the role of metallic impurities and the distribution of N-functionalities on ORR electrocatalysts are still very much under discussion. The contribution of transition metal impurities on overall ORR catalyst activity has been repeatedly reported [29,57]. However, the high activity of our catalyst cannot be related to metal impurities, as no evidence from residual Co catalyst particles was detected by XPS, HR-TEM and electrochemical methods.

It is known that synthesis conditions such as temperature, nitrogen precursor, feed gas composition and metal catalysts strongly affect the type and amount of N-functionalities in the doped material [41,58–60]. Despite extensive research, it is not yet established whether pyridinic-N, pyrrolic-N or graphitic-N sites are the most active for ORR, as inferred from Table 3. Theoretical calculations have also suggested that nitrogen-doped Stone–Wales defects can effectively reduce the energy barrier of oxygen dissociation on N-CNTs [5,61]. In this work, the ORR activity of N-FWCNTs produced by carbonization at 900 °C is the highest (Fig. 5b), which can be attributed to a higher graphitic-N content (~45%) compared to that of NFW-F-600 (~20%). Furthermore, although the difference in doping levels is very small, there is a higher proportion of graphitic-N in NFW-F-900 than in NFW-Pr-900, corresponding to a higher catalytic activity. Our DFT calculations have also shown that with increasing graphitic-N atoms in N-CNTs, the energy barrier of oxygen adsorption decreases [26].

The small diameter of the FWCNT support may also contribute to the excellent ORR activity. In Table 3, another column shows the diameter of N-CNTs from literature compared to that of our N-FWCNTs. As can be seen, our FWCNTs have significantly smaller diameters (1.8–7.7 nm) than the most reported N-CNTs (25–200 nm). DFT calculations have indicated that the diameter of CNTs has an important effect on the oxygen dissociation activation energy barrier. Narrower N-CNTs exhibit a lower activation barrier for  $\text{O}_2$  dissociation, resulting in better ORR catalytic activity [26,62]. There are not yet supporting experimental studies in

literature regarding the effect of diameter of N-CNTs on the ORR activity of N-doped CNTs.

## 5. Conclusions

High catalytic activity for the oxygen reduction reaction (ORR) was achieved by a post-treatment of few-walled carbon nanotubes (FWCNTs) with polyaniline, followed by pyrolysis at high temperatures. Despite significantly lower nitrogen content (~0.5 at.%) compared to the literature, the resulting nitrogen-containing FWCNTs (N-FWCNTs) showed remarkable electrocatalytic activity for ORR. N-FWCNTs also showed a high activity for the hydrogen evolution reaction and hydrogen peroxide decomposition, suggesting that the active sites involved in the ORR can simultaneously catalyze other reactions at different potentials. The high activity for such a low N-content could be explained by the exceptional accessibility for the catalytic sites located in the open and porous N-doped layer surrounding the FWCNT core, along with the minimization of inactive inner volume and mass compared to larger multi-walled nanotubes.

## Acknowledgements

The authors would like thank the following instances for funding: Academy of Finland (12263636). Aalto University Starting Grant and MIDE (GRACE) and Alfred Kordelin Foundation. This work made use of the Aalto University Nanomicroscopy Center (Aalto-NMC) premises. M.B. is also thankful to Dr. Ivar Kruusenberg for the kind help with experiments in the laboratory of Tartu University. We also acknowledge support by the Estonian Research Council (IUT20-16).

## Appendix A. Supplementary data

Supplementary material related to this article can be found, in the online version, at <http://dx.doi.org/10.1016/j.apcatb.2014.04.027>.

## References

- [1] Y. Wang, K.S. Chen, J. Mishler, S.C. Cho, X.C. Adroher, *Appl. Energy* 88 (2011) 981–1007.
- [2] X. Zhao, M. Yin, L. Ma, L. Liang, C. Liu, J. Liao, T. Lu, W. Xing, *Energy Environ. Sci.* 4 (2011) 2736–2753.
- [3] E.H. Yu, X. Wang, U. Krewer, L. Li, K. Scott, *Energy Environ. Sci.* 5 (2012) 5668–5680.
- [4] X. Sun, P. Song, Y. Zhang, C. Liu, W. Xu, W. Xing, *Sci. Rep.* 3 (2013) 1–5.
- [5] K. Gong, F. Du, Z. Xia, M. Durstock, L. Dai, *Science* 323 (2009) 760–764.
- [6] T. Susi, A. Kaskela, Z. Zhu, P. Ayala, R. Arenal, Y. Tian, P. Laiho, J. Mali, A.G. Nasibulin, H. Jiang, G. Lanzani, O. Stephan, K. Laasonen, T. Pichler, A. Loiseau, E.I. Kauppinen, *Chem. Mater.* 23 (2011) 2201–2208.
- [7] S. Kundu, T.C. Nagaiah, W. Xia, Y. Wang, S.V. Dommele, J.H. Bitter, M. Santa, G. Grundmeier, M. Bron, W. Schuhmann, M. Muhler, *J. Phys. Chem. C* 113 (2009) 14302–14310.
- [8] Z. Chen, D. Higgins, Z. Chen, *Electrochim. Acta* 55 (2010) 4799–4804.
- [9] T. Sharifi, F. Nitze, H.R. Barzegar, C.-W. Tai, M. Mazurkiewicz, A. Malolepszy, L. Stobinski, T. Wågberg, *Carbon* 50 (2012) 3535–3541.
- [10] D. Geng, H. Liu, Y. Chen, R. Li, X. Sun, S. Ye, S. Knights, *J. Power Sources* 196 (2011) 1795–1801.
- [11] T.C. Nagaiah, S. Kundu, M. Bron, M. Muhler, W. Schuhmann, *Electrochem. Commun.* 12 (2010) 338–341.
- [12] G. Liu, X. Li, P. Ganesan, B.N. Popov, *Electrochim. Acta* 55 (2010) 2853–2858.
- [13] C. Jin, T.C. Nagaiah, W. Xia, B. Spliethoff, S. Wang, M. Bron, W. Schuhmann, M. Muhler, *Nanoscale* 2 (2010) 981–987.
- [14] M. Vikkisk, I. Kruusenberg, U. Joost, E. Shulga, K. Tammeveski, *Electrochim. Acta* 87 (2013) 709–716.
- [15] J. Yin, Y. Qiu, J. Yu, *Chem. Lett.* 42 (2013) 413–415.
- [16] H.-S. Oh, J.-G. Oh, B. Roh, I. Hwang, H. Kim, *Electrochem. Commun.* 13 (2011) 879–881.
- [17] M. Vikkisk, I. Kruusenberg, U. Joost, E. Shulga, I. Kink, K. Tammeveski, *Appl. Catal. B: Environ.* 147 (2014) 369–376.
- [18] L. Qu, Y. Liu, J.-B. Baek, L. Dai, *ACS Nano* 4 (2010) 1321–1326.
- [19] R. Liu, D. Wu, X. Feng, K. Müllen, *Angew. Chem. Int. Ed.* 49 (2010) 2565–2569.



- [20] S. Chen, J. Bi, Y. Zhao, L. Yang, C. Zhang, Y. Ma, Q. Wu, X. Wang, Z. Hu, *Adv. Mater.* 24 (2012) 5593–5597.
- [21] G. Ma, R. Jia, J. Zhao, Z. Wang, C. Song, S. Jia, Z. Zhu, *J. Phys. Chem. C* 115 (2011) 25148–25154.
- [22] K. Chizari, A. Deneuve, O. Ersen, I. Florea, Y. Liu, D. Edouard, I. Janowska, D. Begin, C. Pham-Huu, *ChemSusChem* 5 (2012) 102–108.
- [23] D. Yu, E. Nagelli, F. Du, L. Dai, *J. Phys. Chem. Lett.* 1 (2010) 2165–2173.
- [24] J.D. Wiggins-Camacho, K.J. Stevenson, *J. Phys. Chem. C* 113 (2009) 19082–19090.
- [25] M. Terrones, A.S. Filho, A. Rao, *Carbon Nanotubes*, Springer, Berlin, Heidelberg, 2008, pp. 531–566.
- [26] D. Srivastava, T. Susi, M. Borghei, L. Kari, *RSC Adv.* 4 (2014) 15225–15235.
- [27] C.V. Rao, C.R. Cabrera, Y. Ishikawa, *J. Phys. Chem. Lett.* 1 (2010) 2622–2627.
- [28] C. Venkateswara Rao, Y. Ishikawa, *J. Phys. Chem. C* 116 (2012) 4340–4346.
- [29] J.D. Wiggins-Camacho, K.J. Stevenson, *J. Phys. Chem. C* 115 (2011) 20002–20010.
- [30] S. Ratso, I. Kruusenberg, M. Vikkisk, U. Joost, E. Shulga, I. Kink, T. Kallio, K. Tammeveski, *Carbon* 73 (2014) 361–370.
- [31] A.U. Haq, J. Lim, J.M. Yun, W.J. Lee, T.H. Han, S.O. Kim, *Small* 9 (2013) 3829–3833.
- [32] H. Zhong, H. Zhang, Z. Xu, Y. Tang, J. Mao, *ChemSusChem* 5 (2012) 1698–1702.
- [33] G. Wu, K.L. More, C.M. Johnston, P. Zelenay, *Science* 332 (2011) 443–447.
- [34] E.N. Konyushenko, J. Stejskal, M. Trchová, J. Hradil, J. Kovářová, J. Prokeš, M. Cieslar, J.-Y. Hwang, K.-H. Chen, I. Sapurina, *Polymer* 47 (2006) 5715–5723.
- [35] Y. Feng, H. Zhang, Y. Hou, T.P. McNicholas, D. Yuan, S. Yang, L. Ding, W. Feng, J. Liu, *ACS Nano* 2 (2008) 1634–1638.
- [36] S. Latil, S. Roche, D. Mayou, J.-C. Charlier, *Phys. Rev. Lett.* 92 (2004) 256805.
- [37] E.G. Rakov, D.A. Grishin, Yu.V. Gavrilov, E.V. Rakova, A.G. Nasibulin, H. Jiang, E.I. Kauppinen, *Russ. J. Phys. Chem.* 78 (2004) 6.
- [38] L. Li, Z.-Y. Qin, X. Liang, Q.-Q. Fan, Y.-Q. Lu, W.-H. Wu, M.-F. Zhu, *J. Phys. Chem. C* 113 (2009) 5502–5507.
- [39] P. Kanninen, M. Borghei, O. Sorsa, E. Pohjalainen, E.I. Kauppinen, V. Ruiz, T. Kallio, *Appl. Catal. B: Environ.* 156–157 (2014) 341–349, <http://dx.doi.org/10.1016/j.apcatb.2014.03.041>.
- [40] M.S. Dresselhaus, G. Dresselhaus, R. Saito, A. Jorio, *Phys. Rep.* 409 (2005) 53.
- [41] T. Sharifi, G. Hu, X. Jia, T. Wågberg, *ACS Nano* 6 (2012) 8904–8912.
- [42] J.R. Pels, F. Kapteijn, J.A. Moulijn, Q. Zhu, K.M. Thomas, *Carbon* 33 (1995) 13.
- [43] R. Arrigo, M. Havecker, R. Schlögl, D.S. Su, *Chem. Commun.* 40 (2008) 4891–4893.
- [44] C. Song, J. Zhang, in: J. Zhang (Ed.), *PEM Fuel Cell Electrocatalysts and Catalyst Layers*, Springer, London, 2008, pp. 89–134.
- [45] A.J. Bard, L.R. Faulkner, *Electrochemical methods*, 2nd ed., Wiley, 2001, chap. 3, pp. 101–3.
- [46] F.d.r. Jaouen, J.-P. Dodelet, *J. Phys. Chem. C* 113 (2009) 15422–15432.
- [47] J.M. Goran, J.L. Lyon, K.J. Stevenson, *Anal. Chem.* 83 (2011) 8123–8129.
- [48] A. Santasalo-Aarnio, S. Hietala, T. Rauhala, T. Kallio, *J. Power Sources* 196 (2011) 6153–6159.
- [49] Z. Chen, D. Higgins, Z. Chen, *Carbon* 48 (2010) 3057–3065.
- [50] Z. Chen, D. Higgins, H. Tao, R.S. Hsu, Z. Chen, *J. Phys. Chem. C* 113 (2009) 21008–21013.
- [51] H.-S. Oh, J.-G. Oh, W.H. Lee, H.-J. Kim, H. Kim, *Int. J. Hydrogen Energy* 36 (2011) 8181–8186.
- [52] Z. Wang, R. Jia, J. Zheng, J. Zhao, L. Li, J. Song, Z. Zhu, *ACS Nano* 5 (2011) 1677–1684.
- [53] M. Reyes-Reyes, N. Grobert, R. Kamalakaran, T. Seeger, D. Golberg, M. Rühle, Y. Bando, H. Terrones, M. Terrones, *Chem. Phys. Lett.* 396 (2004) 167–173.
- [54] R.A. Sidik, A.B. Anderson, N.P. Subramanian, S.P. Kumaraguru, B.N. Popov, *J. Phys. Chem. B* 110 (2006) 1787–1793.
- [55] M. Lefèvre, E. Proietti, F. Jaouen, J.-P. Dodelet, *Science* 324 (2009) 71–74.
- [56] F. Jaouen, M. Lefèvre, J.-P. Dodelet, M. Cai, *J. Phys. Chem. B* 110 (2006) 5553–5558.
- [57] Y. Li, W. Zhou, H. Wang, L. Xie, Y. Liang, F. Wei, J.-C. Idrobo, S.J. Pennycook, H. Dai, *Nat. Nano.* 7 (2012) 394–400.
- [58] H. Niwa, K. Horiba, Y. Harada, M. Oshima, T. Ikeda, K. Terakura, J.-i. Ozaki, S. Miyata, *J. Power Sources* 187 (2009) 93–97.
- [59] T.C. Nagaiah, A. Bordoloi, M.D. Sánchez, M. Muhler, W. Schuhmann, *ChemSusChem* 5 (2012) 637–641.
- [60] W.Y. Wong, W.R.W. Daud, A.B. Mohamad, A.A.H. Kadhun, E.H. Majlan, K.S. Loh, *Diam. Relat. Mater.* 22 (2012) 12–22.
- [61] B. Shan, K. Cho, *Chem. Phys. Lett.* 492 (2010) 131–136.
- [62] S. Ni, Z. Li, J. Yang, *Nanoscale* 4 (2012) 1184–1189.